Chemical routes to materials

Enhanced photocatalytic degradation of norfloxacin under visible light by immobilized and modified In$_2$O$_3$/TiO$_2$ photocatalyst facilely synthesized by a novel polymeric precursor method

Han Yu[1,2] , Fenghua Chen[1,2,*] , Li Ye[1,2] , Heng Zhou[1,2] , and Tong Zhao[1,2,*]

[1] *Laboratory of Advanced Polymeric Materials, Institute of Chemistry, Chinese Academy of Sciences, Beijing 100190, People's Republic of China*
[2] *University of Chinese Academy of Sciences, Beijing 100049, People's Republic of China*

ABSTRACT

Ion co-doped photocatalysts with In$_2$O$_3$/TiO$_2$ heterostructure (In$_2$O$_3$/TiO$_2$(m)) were prepared through a new polymeric precursor method. The In$_2$O$_3$/TiO$_2$(m) precursor solution is of salient advantage in coating photocatalysts on various substrates and multiple modifications. The photocatalysts were facilely obtained after the calcination of precursors. Mass ratio of In/Ti was optimized according to their photocatalytic performances, and IT(m)-3 ($w_{In/Ti}$ = 3%, modified by N, B co-doping) showed the best photocatalytic activity. The band gap was successfully narrowed to 2.37 eV, and In$_2$O$_3$/TiO$_2$ heterostructure was successfully constructed in the photocatalysts. Visible light absorption and separation of photoexcited carriers were significantly enhanced. Under visible light, NOX (20 mg/L in the water) was 100% photodegraded in 10 min, with 100% TOC removed in 25 min. The IT(m)-3-loaded quartz fabrics (ITQ) also showed excellent photocatalytic performance. The photocatalytic activity of ITQ was repeatable and stable in 45 rounds of recycle without centrifugation. Synergetic effect of heterostructure and element doping was considered contributing to the outstanding photocatalysis performance. The polymeric precursor method proposed in this work showed great potential in large-scale preparation and application of immobilized photocatalysts. The synergetic improvement through co-modifications showed its proper compatibility with modifications.

Address correspondence to E-mail: fhchen@iccas.ac.cn; tzhao@iccas.ac.cn

Springer

Introduction

Antibiotics have been utilized as an elixir to protect human beings and animals from various pathogens for more than a half of century, and the production and consumption are both escalating in recent years [1]. The emission of antibiotics from hospitals and farms is increasingly detrimental to water environments [2–4]. Norfloxacin (NOX), belonging to the third generation of fluoroquinolone antibiotics (FQAs), has been repeatedly found in various aqueous environments [5–8]. The omnipresent and increasing concentration of NOX in aquatic environments may induce occurrence of microbial pathogens with antibiotic resistance, rendering the extant antibiosis treatment futile [9–12]. In order to remove the antibiotics from wastewater, numerous techniques have been exerted, such as microbial degradation process [13], sorption [5, 14, 15] or Fenton process [16]. However, due to the stability and poor biodegradability of the quinolone ring of NOX [17], traditional treatment cannot achieve efficient degradation of NOX or demands tremendous time and money [18].

Recently, photocatalysis has been receiving considerable concern as an effectual method in the field of water treatment [19–23], which is able to overcome the disadvantages of low efficient degradation and secondary pollution for its complete degradation of organic contaminates into H_2O and CO_2 [24–26]. TiO_2 is generally recognized as the promising photocatalyst for its nontoxicity, stability, low-cost and high photocatalytic activity [27]. However, pristine TiO_2 shows hardly any photocatalysis under visible light due to its intrinsic wide band gap (3.2 eV) and frequent recombination of excited carriers during the photodegradation [28]. Therefore, numerous researches have been conducted to improve the visible-light photocatalytic activity and restrain the recombination of photogenerated carriers, such as self-doping [29], ion doping [30–32] and heterojunction constructing [28, 33–36]. The strategy of ion doping is a convenient and fruitful way to narrow the band gap by the substitution of Ti 3d or O 2p states [37]. Moreover, multiple ions co-doping, such as N-B co-doping [38], N–Cl co-doping [39], N–Ir co-doping [40] and N-F co-doping [41], has been studied and proved to be more effective than single-element doping. Besides, heterostructure constructing with

semiconductors with narrow band gap is also an ideal candidate because their typical structure is conducive to charge separation and transfer [42]. Indium oxide, with a band gap of 2.8 eV, is an indirect band semiconductor and known as a transparent conducting material which has been diffusely applied in solar cells and optical or antistatic coatings [43]. Moreover, In_2O_3 has also been proved to be competent in improving the photocatalytic efficiency of other semiconductors by improving absorption of visible light region [44, 45] and In_2O_3/TiO_2 heterostructrue is reported to be in favor of increasing the photocatalytic activity due to the lower bandgap of In_2O_3 and band alignments of both semiconductor materials [46]. Mohammad et al. [47] prepared mesoporous In_2O_3-TiO_2 nanocomposites by a sol–gel method, and the sample 0.1% In_2O_3-TiO_2 achieved the best photocatalytic performance under UV light. However, the product in this work showed no improved visible light absorption in terms of its ultraviolet–visible diffuse reflectance spectra (UVDRS), and no photodegradation efficiencies under visible light were provided. Du et al. [48] prepared core–shell-structured TiO_2@In_2O_3, and it showed enhanced photocatalytic activity under visible light compared with the samples for reference. In_2O_3 significantly enhanced visible-light absorption of TiO_2 and photocatalytic activity of decomposing methyl orange in this work. The final product of the above two studies was in the form of powders or particles, limiting their practical application because the posttreatment recovery of TiO_2 in powder form is both time and money consuming [49]. An et al. [50] prepared immobilized TiO_2@In_2O_3 by a two-step hydrothermal method and adopted photoelectrochemical (PEC) measurements to investigate the capacity of water splitting and degradation of BPA. Though compared with TiO_2 nanorods (NR), the TiO_2@In_2O_3 showed improved photocatalytic performance according to the H_2 evolution reaction (HER) rates; no improvement in photodegradation efficiency can be discerned through PEC decomposition of bisphenol A and methyl orange. Moreover, the UVDRS also showed no redshift to longer wavelength.

Hence, to further improve visible light response and photocatalytic activity of TiO_2, incorporating ion doping and In_2O_3 heterostructures into the co-modification of TiO_2 catalyst is promising, but the common viable approaches of ion doping or

heterostructures in the previous studies demand long synthesis period and harsh condition which is detrimental to further massive production of catalysts, and the form of their products are mainly in powder which severely reduces the feasibility of practical application because of the expensive separation and recycle process for the powdered photocatalysts. Thus, it is imperative for academy and industry to find a convenient and effectual way of the ion doping or heterostructure construction. Feasible processing and stable recyclability will be a bonus for massive production and application in reality.

To resolve these scientific issues, polymeric precursor method [51] can be exerted whose product is homogeneous and long-term stable solution. This approach shows various advantages: (1) adjustable structure and composition; (2) mild synthesis conditions and short synthesis period; (3) facile to various modification and immobilization on substrates; (4) superior film forming ability and uniformity; (5) compatible with soft template to introduce pore structures. Based on the above superiorities, polymeric precursor method is suitable for the preparation of double elements co-doped photocatalyst with heterostructures and substrate-loaded photocatalyst or nanofiber membranes which facilitated the separation and reuse.

In this work, N–B co-doped TiO_2 catalysts with In_2O_3/TiO_2 heterostructure ($In_2O_3/TiO_2(m)$) were prepared by a one-step polymeric precursor method. The physical property and chemical structure were characterized. The results of photodegradation tests showed that the photocatalytic capacity of the powered TiO_2 catalyst and substrate-loaded catalysts were remarkable in decomposing NOX. The mechanism of how N, B co-doping and In_2O_3/TiO_2 heterostructure ameliorated photocatalysis performance was also discussed.

Experiment

Preparation of $In_2O_3/TiO_2(m)$

$In_2O_3/TiO_2(m)$ precursor solution was prepared by polymeric precursor method [51] (Fig. 1). Typically, titanium tetraisopropoxide (TTIP, Aldrich) was mixed with PEG-600 (Xilong Chemical Co. Ltd) and $In(NO_3)_3$ (Aladdin Industrial Co.). The mixture was heated at 120 °C for 2 h with the presence of drastic

stir. After cooling to 90 °C, boric acid (BA, Sinopharm Chemical Reagent Co.) was added in and heated at 110 °C for 4 h. Then, acetamide (Acam, Sinopharm Chemical Reagent Co.) was added in the solution, which was heated at 120 °C for 4 h and then cooled to 85 °C. After that, acetylacetone (Acac, Sinopharm Chemical Reagent Co.) and a mixture of H_2O and n-propanol (Sinopharm Chemical Reagent Co.) (mass ratio of H_2O/n-propanol is 1/4) were sequentially added dropwise. Then, the mixture was refluxed for 2 h to accomplish the preparation of $In_2O_3/TiO_2(m)$ precursor. Afterward, the solvent of as-prepared precursor solution was evaporated and the obtained $In_2O_3/TiO_2(m)$ resins were calcined at 450 °C for 30 min with a heating rate of 3 °C/min. After calcination, the obtained $In_2O_3/TiO_2(m)$ chips were manually ground into powders. The molar ratio of the TTIP/BA/Acam/Acac/H_2O was 1.0/0.24/2.0/0.3/0.5, and the mass ratio of In/Ti varied from 1%, 3% and 5%, denoting as IT(m)-1, IT(m)-3 and IT(m)-5, respectively. Besides, sample IT-10 (In_2O_3/TiO_2 sample without the ion doping, $m_{In}/m_{Ti} = 10\%$), sample $TiO_2(m)$ (TiO_2, co-doped with N and B, without the addition of indium nitrate) and pristine TiO_2 (without the ion doping and the addition of indium nitrate) were also prepared by similar method for comparison.

Preparation of coated quartz fabrics

Quartz fabric (QF) wool was preheated at 450 °C in muffle oven, removing the sizing agent on the surface. The heat-treated QF was tailored to a size of 50 mm × 30 mm as substrate with a weight of 0.15 g controlled by thickness. The IT(m)-3 precursor was diluted with n-propanol, content controlled by Ti mass ratio of 3%, Then, polyvinylpyrrolidone (PVP, 1% of mass of diluted precursor) was added and the system was heated at 100 °C for 1 h. The tailored QF was dipped into the 50 g diluted precursor and heated for 1 h at 100 °C. Then, it was extracted and the solvent was evaporated. The resulting precursor-coated QF was calcined at 450 °C for 30 min; the resulted IT(m)-3 coated-QF labeled as ITQ. The mass of loaded catalysts was 30 mg.

Characterization

Crystalline structures were probed by X-ray diffraction (XRD, Rigaku D/max 2500, Cu Ka source, 40 kV
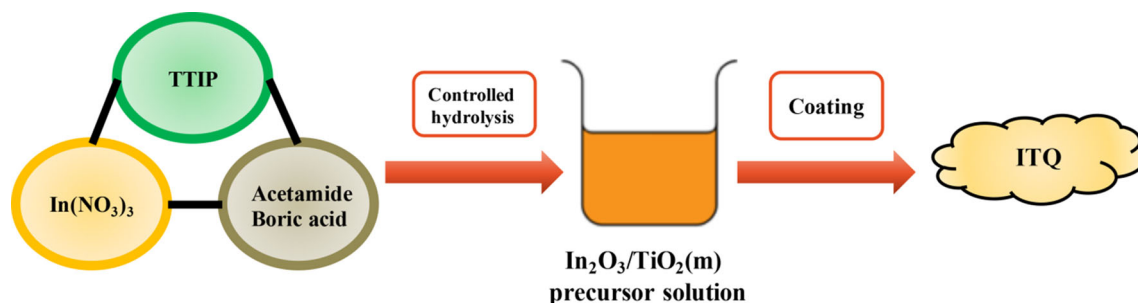
Figure 1 Schematic illustration of preparation process of $In_2O_3/TiO_2(m)$ precursor solution and ITQ.

200 mA). Chemical structure was studied by X-ray photoelectron spectroscopy (XPS, ESCALab220i-XL). The morphology was investigated by a field-emission scanning electron microscope (SEM, Hitachi SU-8020) at an accelerating voltage of 10 kV and a high-resolution field-emission transmission electron microscope (HRTEM, JEOL JEM-2100F) at an accelerating voltage of 200 kV. The contents of titanium and indium in the catalysts were measured by inductively coupled plasma atomic emission spectroscopy (ICP-AES, IRIS Intrepid II XDL, Thermo Electron Corporation), and nitrogen and oxygen content were measured by a nitrogen/oxygen analyzer (TC-306, Baoying Technology). The Brunauer–Emmett–Teller (BET) surface areas of samples were analyzed by nitrogen adsorption by induced isotherms at 77 K with a Micromeritics ASAP 2020 instrument. The photoluminescence (PL) spectra were measured with a fluorescence spectrometer (F-4500, HITACHI). The ultraviolet–visible diffuse reflectance spectra (UV–Vis DRS) were probed by a spectrophotometer (Shimadzu, UV-2600).

Photodegradation of NOX

$In_2O_3/TiO_2(m)$, with 30 mg amount, and ITQ were utilized to catalyze the photodegradation of NOX (20 mg/L, 30 ml) in cuvettes under visible light from a 500-W Xeon lamp (wavelength below 420 nm cut off). After the treatment, ITQ was extracted and repeatedly washed by deionized water. Then, it was dried out at 100 °C and ready for recycle test. The photodegraded samples containing catalyst powders were all centrifuged, while the ones photocatalyzed by immobilized catalysts were separated without the presence of centrifugation. After the separation, the left solutions were analyzed by spectrophotometric method. The total organic carbon (TOC, Shimadzu,

TOC-L) was adopted to measure the mineralization degree of NOX.

Results and discussion

Crystalline structure and morphology

XRD patterns of $In_2O_3/TiO_2(m)$ with different indium contents are shown in Fig. 2. Accordingly, crystal phase of anatase TiO_2 is mainly obtained (ICDD: 01-071-1166). Besides, a relatively small peak at $\sim 30.2°$ is detected compared with the XRD result of the pristine TiO_2 (Figure S1) and supposed to be ascribed to the overlapped Bragg diffraction peak of B_2O_3 and In_2O_3. A minor but nonnegligible shift toward lower 2Theta degree can also be detected as the mass ratio of indium increases (inset of Fig. 1), as is mainly caused by the TiO_2 lattice disruption of In_2O_3/TiO_2 heterostructure. Rietveld fittings were also executed by Xpert Highscore. The results show
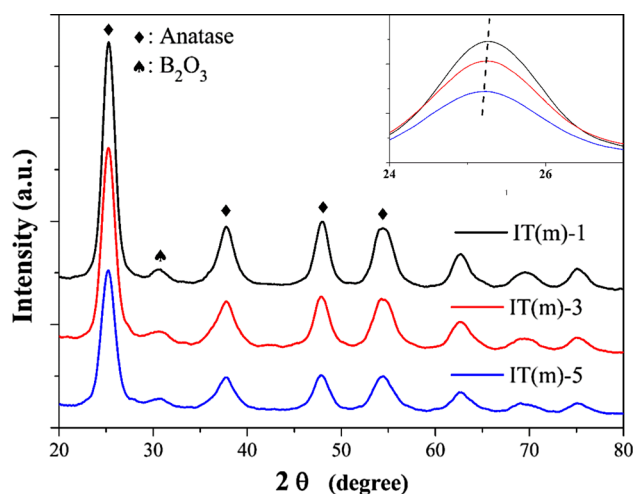

Figure 2 XRD patterns of the $In_2O_3/TiO_2(m)$ samples and local magnification (insert).

that the lattice parameters of sample IT(m)-3 ($a = 3.811$ Å, $b = 3.811$ Å, $c = 9.511$ Å) increase when compared with that of pristine TiO_2 ($a = 3.776$ Å, $b = 3.776$ Å, $c = 9.486$ Å), indicating that nitrogen and boron are successfully introduced into the crystal lattice of TiO_2 since the atomic radius of oxygen are smaller than those of nitrogen and boron [52].

The morphology was investigated by SEM and HRTEM. As shown in the SEM image for sample IT(m)-3 (Fig. 3a), the prepared photocatalysts are uniformly pseudo-spherical nanoparticles and stacked in a botryoidal structure with brain-textured sulci and gyri. The elemental mapping analysis result of IT(m)-3 (Figure S2) shows that the added elements are present in the sample and they are homogeneously dispersed on the TiO_2. Also, the uniformity of particle size is favorable, ranging from 10 to 20 nm, and in conformity to the diameter of P25, the mainstream TiO_2 commodity [28]. Interestingly, the BET surface area of IT(m)-3 is 206.89 m^2/g which is 3.4 times larger than that of P25 (60.44 m^2/g), the N_2 adsorption–desorption isotherm of IT(m)-3 and its pore size distribution (Figure S3) indicate that mesoporous structure was formed during the calcination which is reported to be able to be beneficial for visible light absorption [53], additional active sites and higher electron transfer capacities [54]. HRTEM images (Fig. 3c, d) distinctly show the lattice fringes spacing of 0.35 nm, which is in correspondence with (101) facet of anatase [55]. Besides, the discernable lattice fringes spacing of 0.41 nm is in agreement with (211) facet of cubic In_2O_3 coupled with the (101) facet of anatase [56]. As a control, HRTEM image of IT-10 (Fig. 3b) shows distinct attachment of lattice fringes of anatase (0.35 nm) and cubic In_2O_3 (0.41 nm). Thus, the In_2O_3/TiO_2 heterostructure is well established and it is reported that heterostructure is conducive to better charge separation via acting as trapping site and phase-junction [33]. The crystal phase structure obtained by HRTEM images is consistent with that obtained from XRD analysis.

Chemical composition and structure

ICP-AES and nitrogen/oxygen analyzer were exerted to measure the metal and nonmetallic element contents in the catalysts, respectively. Based on the results shown in Table S1, the mass ratio of In/Ti for the sample IT(m)-3 is $\sim$ 3% which is identical with the raw mass ratio of In/Ti in preparation, indicating
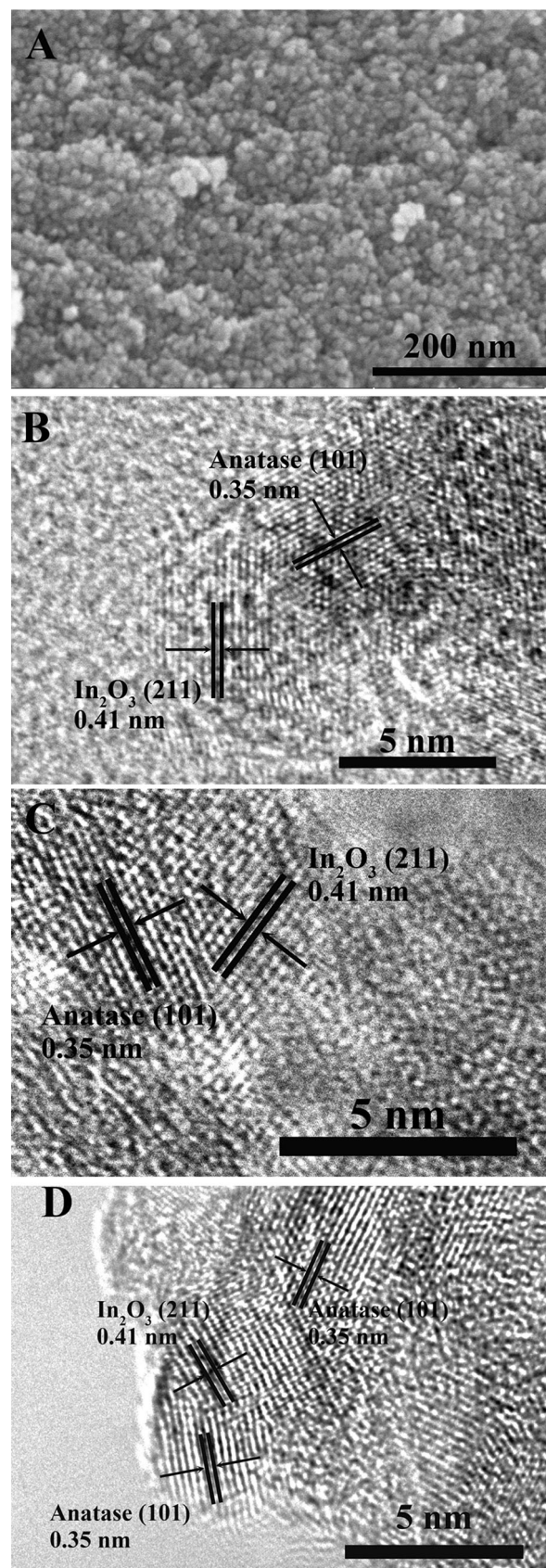
◄**Figure 3** SEM image of IT(m)-3 (**a**), HRTEM images of IT-10 (**b**) and IT(m)-3 (**c, d**).

that there is nearly no attrition of indium during the preparation.

X-ray photoelectron spectroscopy was used to investigate chemical structures of the sample IT(m)-3, and the chemical environments of N, B, In and Ti were obtained, as shown in Fig. 4. The N 1 s XPS spectrum (Fig. 5a) shows two peaks located at 399.34 eV and 397.49 eV after the deconvolution. The peak at 399.34 eV is ascribed to the structure of Ti-N-B [57] and independent interstitial N-doping [39, 58, 59] in the TiO_2 crystal lattice, and the relatively smaller peak at 397.49 eV can be ascribed to the substitutional N-doping in the TiO_2 crystal lattice [60]. The presence of above structures is reported to be conducive to the enhancement of photocatalytic activity of TiO_2 under visible light. The B 1 s spectrum (Fig. 5b) is deconvoluted into two peaks corresponding to the binding energies of 192.04 eV and 193.99 eV which are attributed to the structure of Ti–O–B (interstitial B) [61] and B_2O_3 [62], respectively. The results from N 1 s and B 1 s XPS spectra indicate that the structure of Ti–N–B–O–Ti is generated during the doping, where N and B are co-interstitial in one lattice, and the independent interstitial B, interstitial and substitutional N are also introduced into the TiO_2 crystal lattice. Moreover, the existence of B_2O_3 on the surface confirmed by B 1 s XPS spectrum result is in agreement with XRD results. As shown in Fig. 5C, the In $3d_{5/2}$ XPS spectrum can only be
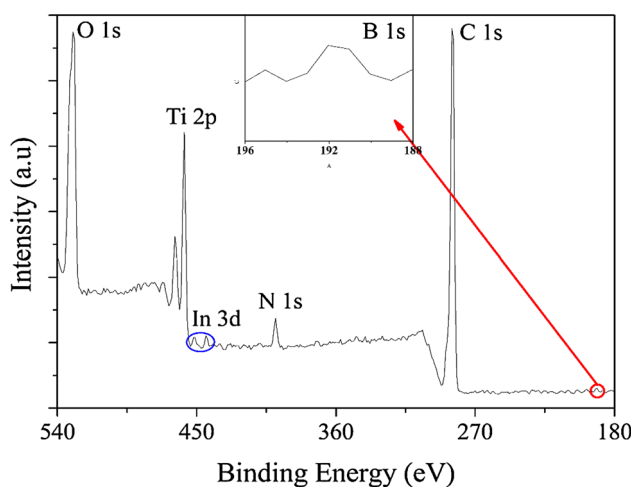
deconvoluted into one peak located at 444.39 eV belonging to In_2O_3 [63]. There are no peaks of In-N or In-B detected, indicating that indium is only present in the form of In_2O_3. According to the Ti 2p XPS spectrum displayed in Fig. 5D, characteristic peaks of Ti $2p_{1/2}$ and Ti $2p_{3/2}$ of the sample IT(m)-3 are located at 464.24 and 458.49 eV, respectively. Difference between the two characteristic peaks (5.75 eV) demonstrated that Ti is in the form of Ti^{4+} [46]. As a comparison, Ti $2p_{1/2}$ and Ti $2p_{3/2}$ peaks of the pristine TiO_2 are located at 465.04 eV and 459.37 eV, respectively. Binding energies of Ti $2p_{1/2}$ and Ti $2p_{3/2}$ peaks of IT(m)-3 are 0.8 eV and 0.88 eV lowered compared with those of pristine TiO_2, respectively; while the splitting to Ti $2p_{1/2}$ and Ti $2p_{3/2}$ is unchanged [28]. The shift can be ascribed to the generation of In_2O_3/TiO_2 heterostructure which leads to the change of chemical environment.

Photodegradation performance

The photocatalytic activities of as-prepared In_2O_3/TiO_2(m) samples were tested by catalyzing the photodegradation of NOX. Figure S4A shows that the sample IT(m)-3 can achieve nearly complete decomposition of NOX after the illumination of visible light for 10 min which is higher than the photodegradation efficiencies of the sample IT(m)-1 and IT(m)-5, showing the marvelous photodegradation efficiency of IT(m)-3. As for the photodegradation results shown in Fig. 6a, about 68% NOX is photodegraded when catalyzed by TiO_2(m); and less than 40% NOX can be photodegraded in the case of IT-10 and pristine TiO_2. IT-10 and IT(m) both show inferior photocatalysis under visible light compared with that of IT(m)-3, indicating that the synergistic effect of ion doping and heterostructures is advantageous. Meanwhile, according to the results of pseudo first-order kinetic curves of NOX decomposition (Figure S4B), the calculated reaction rate constant (k) of IT(m)-3 is the highest, which is 2.46 and 6.52 times more than those of TiO_2(m) and IT-10, respectively. Moreover, TOC was applied in this work to investigate the capacity of mineralization. As shown in Fig. 5B, under visible light, only 11%, 68% and 35% TOC are removed by the pristine TiO_2, TiO_2(m) and IT-10, respectively. 100% TOC removal rate is accomplished by the sample IT(m)-3 under the same condition, indicating its enhanced capacity of mineralization by the synergistic effect of ion doping and
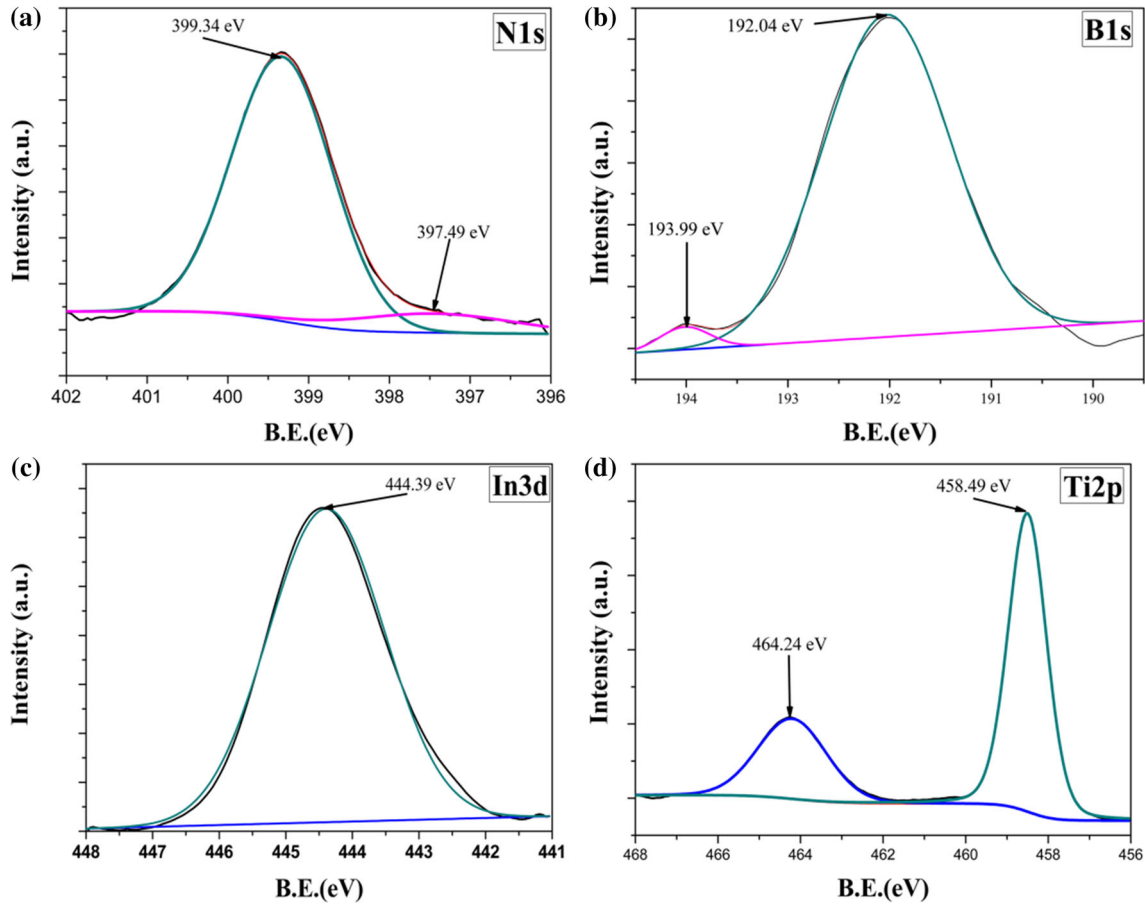

Figure 4 XPS survey spectrum of IT(m)-3.

Figure 5 High-resolution XPS spectra of N 1 s (**a**), B 1 s (**b**), In 3d (**c**), Ti 2p (**d**) of IT(m)-3.
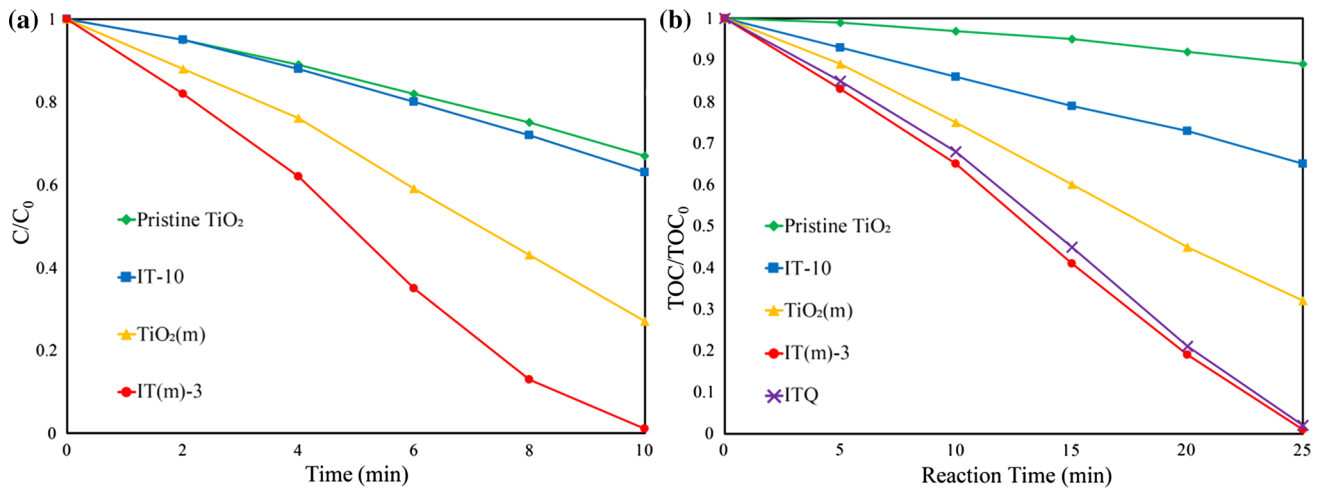

Figure 6 a Time profiles of photocatalytic decomposition of NOX by IT(m)-3 and control samples under visible light; **b** time profiles of the change of TOC in photocatalytic decomposition of NOX by IT(m)-3, ITQ and control samples under visible light.

In_2O_3/TiO_2 heterostructure. After loading the photocatalysts on quartz fabrics, as the sample ITQ prepared, photodegradation experiments can be carried out more conveniently, faster and more efficiently. In

this case, photocatalytic activity and recyclability of ITQ were tested by cycling photodegradation of NOX. As the results shown in Fig. 7, in the 45 rounds of recycle experiments, nearly 100% NOX is
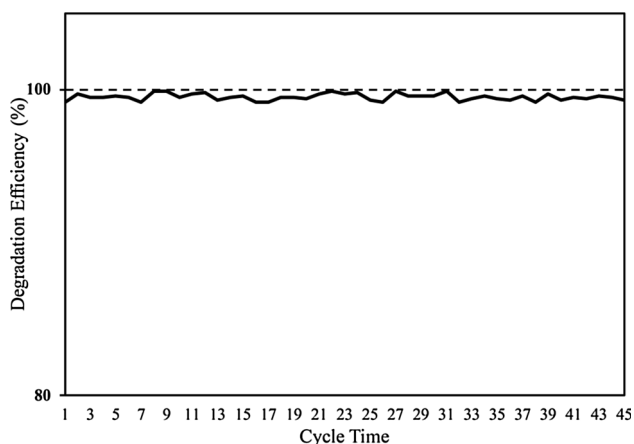
Figure 7 Cycling tests of photodegradation of NOX catalyzed by ITQ under visible light.

Figure 8 UVDRS spectra of the sample IT(m)-3, IT-10, $TiO_2(m)$ and pristine TiO_2.

decomposed at every turn. TOC result of ITQ (Fig. 6b) shows that 100% TOC is also removed in 25 min under visible light. Moreover, XRD pattern of ITQ (Figure S5) shows that anatase is still the dominate crystal phase of the supported photocatalysts and when compared to XRD pattern of pure quartz fabric (Figure S5 inset), the peak located at between 20° and 25° was belonging to quartz fabric, and the rest of it was overlapped by the main diffraction peak (2Theta = 25.2°) of the coated photocatalysts. SEM images of ITQ (Figure S6A, B) indicates that the photocatalysts were uniformly loaded on the quartz fabrics and maintained their crystal phase and morphology after coating process and after the recycling tests, ITQ retains its morphology (Figure S6C, D), indicating the existence of excellent binding force between the loaded IT(m)-3 and the substrates. The high photodegradation efficiency, robust recyclability, simple and convenient maneuverability endowed the ITQ with great potential in massive practical application.

Optical property

UV–Vis diffuse reflectance spectrometer was exerted to investigate photon harvest capacity of the as-prepared catalysts [52]. As the results shown in Fig. 8, all absorption edges of IT(m)-3, IT-10 and $TiO_2(m)$ display evident redshift from ∼ 380 nm of the pristine TiO_2 to ∼ 435, ∼ 455 and ∼ 420 nm, respectively. At the wavelengths after the absorption edges, the three samples, IT(m)-3, IT-10 and $TiO_2(m)$, still possess light absorption, where optical absorption of pristine TiO_2 can be negligible in fact. Among these
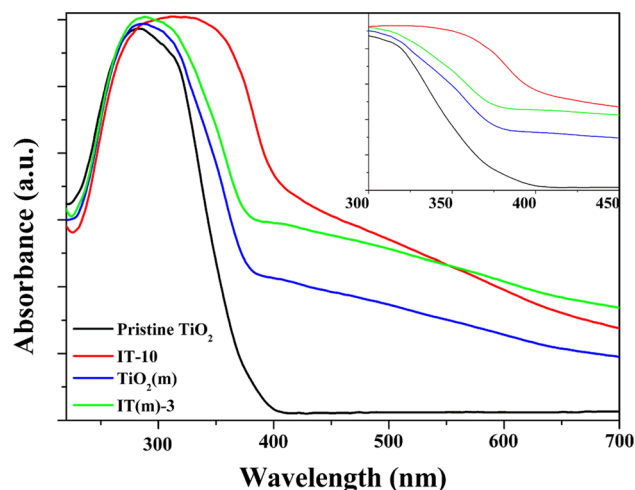
three samples, $TiO_2(m)$ shows lowest light absorption in the whole visible-light region. From their absorption edges to 550 nm, IT-10 shows higher light absorption than IT(m)-3; while at longer wavelengths, absorbance of IT(m)-3 exceeds that of IT-10. It is notable that on the one hand, 10 wt% In was used in the sample IT-10, where absorption edge wavelength more than those of the other samples is realized; on the other hand, although only 3 wt% In was added in IT(m)-3, better absorbance stability is obtained over the visible light range, as mainly contributed from the ion doping.

Meanwhile, Tauc Eq. (1) was exerted to calculate the band gap of these samples [64].

$$(\alpha h v)^{0.5} = k * (h v - E_g) \qquad (1)$$

where α is absorption coefficient, h is Plank constant, v is photon frequency, k is a constant related to the type of transition and E_g is the optical band gap.

As demonstrated in Fig. 9, the band gaps of IT(m)-3, IT-10 and $TiO_2(m)$ are 2.37, 2.24 and 2.64 eV, respectively, which are all narrowed compared to the pristine TiO_2. Although IT(m)-3 is not the best in each single contrast of absorption edge and band gap, it shows the best photocatalytic performance among these samples. Ion doping and heterostructure are, respectively, realized in the $TiO_2(m)$ and IT-10 samples, but synchronously established in the IT(m)-3 sample. It suggests that the ion doping and establishment of In_2O_3/TiO_2 heterostructure are both conducive to the reduction in band gap and enhancement of visible light absorption
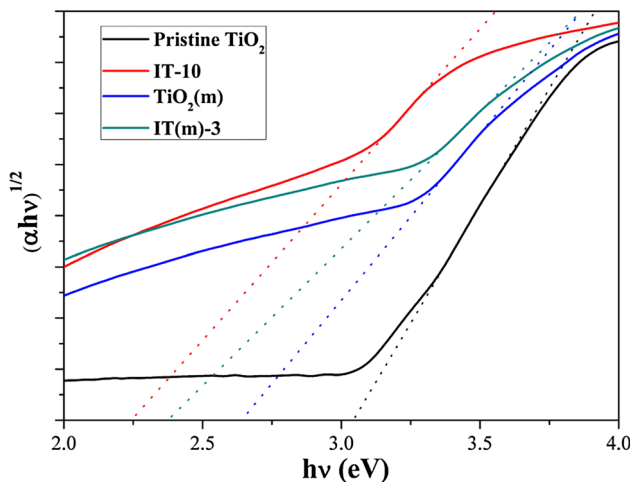
Figure 9 Plots of $(\alpha h\nu)^{0.5}$ versus $h\nu$ of IT(m)-3, IT-10, $TiO_2(m)$ and pristine TiO_2.

simultaneously; combination of the two approaches can make a synergetic effect, resulting in the superior photon reaping capacity of IT(m)-3 under visible light.

The photoluminescence (PL) spectrum indicates the recombination rate of photoexcited carriers by measuring the emission intensity from the secondary combination of these charge carriers [65, 66]. As shown in Fig. 10, the PL intensity of pristine TiO_2 is the highest; it lowers much for IT-10 and $TiO_2(m)$. Moreover, it is notable that the PL intensity of IT(m)-3 is much lower than that of any other sample. For the pristine TiO_2 sample, the fast recombination rate of photoexcited carriers naturally appears without
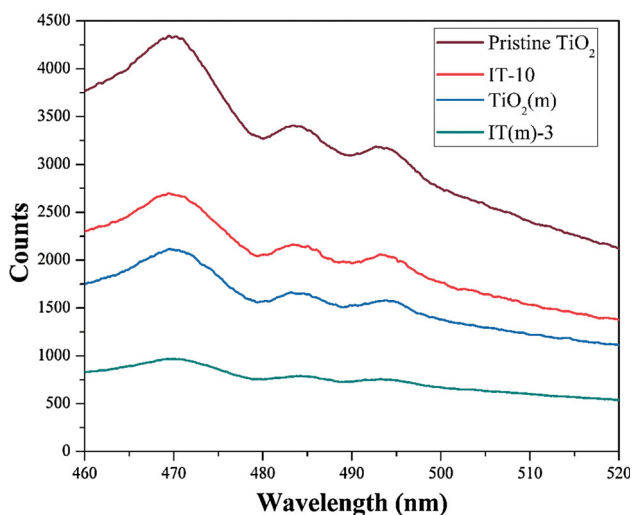

Figure 10 PL spectra of sample IT(m)-3 and the control samples (excited at 280 nm, 20 °C).

obstruction. In the case of IT-10, In_2O_3/TiO_2 heterostructure is established, hindering the recombination of photogenerated electron–hole pairs due to preferable separation and transfer efficiency on the In_2O_3/TiO_2 interface. In the sample $TiO_2(m)$, N and B co-doping structure was constructed and band gap was narrowed. Recombination of charge carriers can also be effectually impeded by the augmented number and shortened migration time of the charge carriers. When the sample IT(m)-3 is used, the combination of ion doping and heterostructure construction generates synergistic positive effect on impeding the recombination of electron–hole pairs. Thus, from an optical point of view, the superior photocatalysis performance of IT(m)-3 is ascribed to the competent absorption in the whole visible-light area and substantially lowered recombination rate of photoexcited electron–hole pairs, both resulted from its narrowed band gap and incorporated In_2O_3/TiO_2 heterostructure.

Photocatalytic reaction mechanism

Hydroxyl radicals (OH·), superoxide radicals ($\cdot O^{2-}$) and holes (h^+) are the main reactive species when TiO_2 photocatalyst is used to catalyze the degradation of NOX. Therefore, to fathom the photocatalytic mechanism of IT(m)-3, three different trapping agents, including EDTA-2Na as holes scavenger [67], tertiary butanol as OH· scavenger [68] and p-benzoquinone as $\cdot O^{2-}$ scavenger [69], were added to gauge their respective effects on the photocatalytic activity of IT(m)-3. According to the results shown in Figure S7, the photodegradation efficiencies of NOX are lowered down to 5%, 88% and 75% when t-butanol, EDTA-2Na and p-benzoquinone were implemented, respectively. The 95% photodegradation efficiency decrease indicates that hydroxyl radicals are the dominate reactive agents of IT(m)-3 when catalyzing the photodegradation of NOX under visible light.

Hence, based on the aforementioned results and band alignment of cubic In_2O_3 and anatase TiO_2 [44, 47, 70, 71], the schematic photodegradation mechanism of IT(m)-3 is proposed and illustrated in Fig. 11. The ion doping narrows the band gap by generating impurity levels above the top of the valence band of TiO_2, improving the visible-light absorption [46], and the In_2O_3/TiO_2 heterostructure favors the separation and transfer of excited electrons of holes on the interface. Specifically, under the

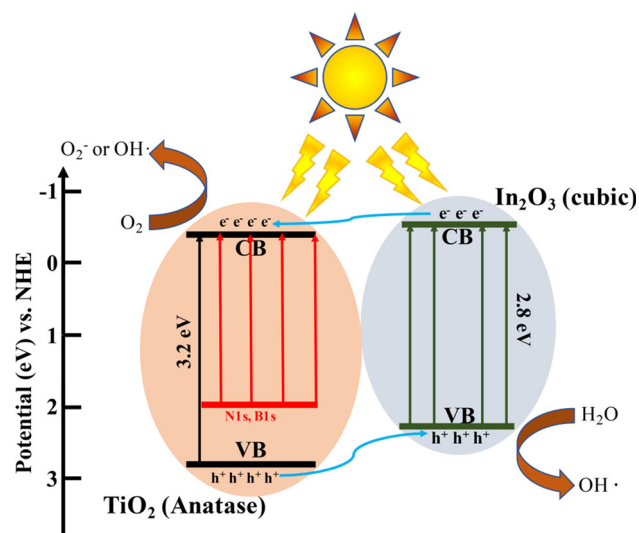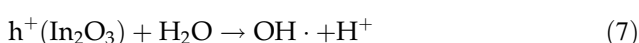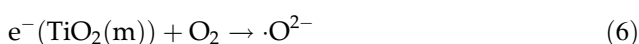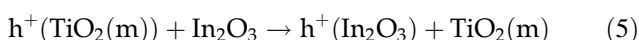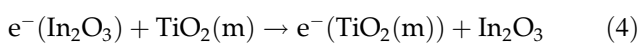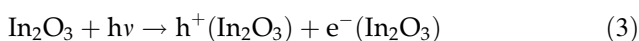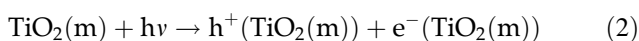**Figure 11** Schematic illustration of photocatalysis mechanism of $In_2O_3/TiO_2(m)$.

irradiation of visible light, modified TiO_2 due to its narrowed band gap and In_2O_3 will generate charge carriers, and since the conduction band potential of TiO_2 is more negative than that of In_2O_3, the generated electrons will transfer to the conduction band of TiO_2. Also, the generated holes in the TiO_2 will also migrate to the valence band of In_2O_3 because its lower valence band potential. The proposed photodegradation mechanism of IT(m)-3 under visible light may function as follows:

$$TiO_2(m) + h\nu \rightarrow h^+(TiO_2(m)) + e^-(TiO_2(m)) \quad (2)$$

$$In_2O_3 + h\nu \rightarrow h^+(In_2O_3) + e^-(In_2O_3) \quad (3)$$

$$e^-(In_2O_3) + TiO_2(m) \rightarrow e^-(TiO_2(m)) + In_2O_3 \quad (4)$$

$$h^+(TiO_2(m)) + In_2O_3 \rightarrow h^+(In_2O_3) + TiO_2(m) \quad (5)$$

$$e^-(TiO_2(m)) + O_2 \rightarrow \cdot O^{2-} \quad (6)$$

$$h^+(In_2O_3) + H_2O \rightarrow OH \cdot + H^+ \quad (7)$$

$$\cdot O^{2-} + H^+ \rightarrow OH\cdot \quad (8)$$

Thus, the facilitation of both the harvest of photons under visible light and the separation of charge carriers which further enhances the photocatalytic activity are realized simultaneously by the synergistic effect of the ion doping and the In_2O_3/TiO_2 heterostructure.

Conclusion

$In_2O_3/TiO_2(m)$ photocatalyst was prepared by a novel precursor method and showed favorable photocatalytic activity. Under visible light, nearly 100% of NOX could be photodegraded by sample IT(m)-3 in 10 min and 100% TOC was removed in 25 min. The preferable photocatalytic activity of IT(m)-3 is due to the enhancement of specific surface areas, the narrowed band gap and the In_2O_3/TiO_2 heterostructures whose synergistic effect improves the capacity of utilization of visible light and reduces the recombination rate of generated electron–hole pairs.

$In_2O_3/TiO_2(m)$ photocatalysts coated on the quartz fabrics are robust and can sustain superior photocatalytic activity after recycling and reusing for 45 times. It is noteworthy that the condition of the polymeric precursor method is moderate, and the centrifugation is not involved during the recycle process, as is a tremendous benefit for reducing cost of pollution treatment. Furthermore, the as-prepared immobilized catalysts could be prepared in a simple way and compatible with many substrates, owing to the favorable machinability of $In_2O_3/TiO_2(m)$ precursor. Thus, it shows great potential in large-scale treatment of industrial or domestic wastewater. The synergistically enhanced photocatalytic activity of IT(m)-3 through the co-modification was also readily achieved by this method, manifesting its proper compatibility with multiple modifications.

Acknowledgements

Electronic supplementary material: The online version of this article (https://doi.org/10.1007/s10853-019-03636-z) contains supplementary material, which is available to authorized users.

References

[1] Zhang QQ, Ying GG, Pan CG, Liu YS, Zhao JL (2015) Comprehensive evaluation of antibiotics emission and fate in

the river basins of China: source analysis, multimedia modeling, and linkage to bacterial resistance. Environ Sci Technol 49:6772–6782

[2] Sarmah AK, Meyer MT, Boxall AB (2006) A global perspective on the use, sales, exposure pathways, occurrence, fate and effects of veterinary antibiotics (VAs) in the environment. Chemosphere 65:725–759

[3] Zhou LJ, Ying GG, Liu S, Zhao JL, Yang B, Chen ZF, Lai HJ (2013) Occurrence and fate of eleven classes of antibiotics in two typical wastewater treatment plants in South China. Sci Total Environ 452–453:365–376

[4] Zhu YG, Johnson TA, Su JQ, Qiao M, Guo GX, Stedtfeld RD, Hashsham SA, Tiedje JM (2013) Diverse and abundant antibiotic resistance genes in Chinese swine farms. Proc Natl Acad Sci USA 110:3435–3440

[5] Peng H, Feng S, Zhang X, Li Y, Zhang X (2012) Adsorption of norfloxacin onto titanium oxide: effect of drug carrier and dissolved humic acid. Sci Total Environ 438:66–71

[6] Tan F, Sun D, Gao J, Zhao Q, Wang X, Teng F, Quan X, Chen J (2013) Preparation of molecularly imprinted polymer nanoparticles for selective removal of fluoroquinolone antibiotics in aqueous solution. J Hazard Mater 244–245:750–757

[7] Pruden A (2014) Balancing water sustainability and public health goals in the face of growing concerns about antibiotic resistance. Environ Sci Technol 48:5–14

[8] Wammer KH, Korte AR, Lundeen RA, Sundberg JE, McNeill K, Arnold WA (2013) Direct photochemistry of three fluoroquinolone antibacterials: norfloxacin, ofloxacin, and enrofloxacin. Water Res 47:439–448

[9] Dinh QT, Moreau-Guigon E, Labadie P, Alliot F, Teil MJ, Blanchard M, Chevreuil M (2017) Occurrence of antibiotics in rural catchments. Chemosphere 168:483–490

[10] Sharma VK, Johnson N, Cizmas L, McDonald TJ, Kim H (2016) A review of the influence of treatment strategies on antibiotic resistant bacteria and antibiotic resistance genes. Chemosphere 150:702–714

[11] Chen QL, Li H, Zhou XY, Zhao Y, Su JQ, Zhang X, Huang FY (2017) An underappreciated hotspot of antibiotic resistance: the groundwater near the municipal solid waste landfill. Sci Total Environ 609:966–973

[12] Liao P, Zhan Z, Dai J, Wu X, Zhang W, Wang K, Yuan S (2013) Adsorption of tetracycline and chloramphenicol in aqueous solutions by bamboo charcoal: a batch and fixed-bed column study. Chem Eng J 228:496–505

[13] Kümmerer K, Al-Ahmad A, Mersch-Sundermann V (2000) Biodegradability of some antibiotics, elimination of the genotoxicity and affection of wastewater bacteria in a simple test. Chemosphere 40:701–710

[14] Liu W, Zhang J, Zhang C, Ren L (2011) Sorption of norfloxacin by lotus stalk-based activated carbon and iron-doped activated alumina: mechanisms, isotherms and kinetics. Chem Eng J 171:431–438

[15] Sassman SA, Sarmah AK, Lee LS (2007) Sorption of tylosin A, D, and A-aldol and degradation of tylosin A in soils. Environ Toxicol Chem 26:1629–1635

[16] Zhang W, Gao H, He J, Yang P, Wang D, Ma T, Xia H, Xu X (2017) Removal of norfloxacin using coupled synthesized nanoscale zero-valent iron (nZVI) with H_2O_2 system: optimization of operating conditions and degradation pathway. Sep Purif Technol 172:158–167

[17] Liao W, Sharma VK, Xu S, Li Q, Wang L (2017) Microwave-enhanced photolysis of norfloxacin: kinetics, matrix effects, and degradation pathways. Int J Environ Res Public Health 14:1564

[18] Pignatello JJ, Oliveros E, MacKay A (2006) Advanced oxidation processes for organic contaminant destruction based on the fenton reaction and related chemistry. Crit Rev Env Sci Tec 36:1–84

[19] Kumar A, Sharma SK, Sharma G, AaH Al-Muhtaseb, Naushad M, Ghfar AA, Stadler FJ (2019) Wide spectral degradation of Norfloxacin by Ag@BiPO4/BiOBr/BiFeO3 nano-assembly: elucidating the photocatalytic mechanism under different light sources. J Hazard Mater 364:429–440

[20] Kumar A, Rana A, Sharma G, Naushad M, AaH Al-Muhtaseb, Guo C, Iglesias-Juez A, Stadler FJ (2018) high-performance photocatalytic hydrogen production and degradation of levofloxacin by wide spectrum-responsive Ag/Fe3O4 Bridged SrTiO3/g-C3N4 plasmonic nanojunctions: joint effect of Ag and Fe3O4. ACS Appl Mater Interfaces 10:40474–40490

[21] Sharma G, Kumar A, Naushad M, Kumar A, AaH Al-Muhtaseb, Dhiman P, Ghfar AA, Stadler FJ, Khan MR (2018) Photoremediation of toxic dye from aqueous environment using monometallic and bimetallic quantum dots based nanocomposites. J Cleaner Prod 172:2919–2930

[22] Dhiman P, Chand J, Kumar A, Kotnala RK, Batoo KM, Singh M (2013) Synthesis and characterization of novel Fe@ZnO nanosystem. J Alloys Compd 578:235–241

[23] Kumar A, Kumar A, Sharma G, Naushad M, Veses RC, Ghfar AA, Stadler FJ, Khan MR (2017) Solar-driven photodegradation of 17-β-estradiol and ciprofloxacin from waste water and CO_2 conversion using sustainable coal-char/polymeric-g-C3N4/RGO metal-free nano-hybrids. New J Chem 41:10208–10224

[24] Dong H, Guo X, Yang C, Ouyang Z (2018) Synthesis of g-C3N4 by different precursors under burning explosion effect and its photocatalytic degradation for tylosin. Appl Catal B 230:65–76

[25] Wang J, Tang L, Zeng G, Deng Y, Liu Y, Wang L, Zhou Y, Guo Z, Wang J, Zhang C (2017) Atomic scale g-C_3N_4/Bi_2WO_6 2D/2D heterojunction with enhanced photocatalytic degradation of ibuprofen under visible light irradiation. Appl Catal B 209:285–294

[26] Dong S, Ding X, Guo T, Yue X, Han X, Sun J (2017) Self-assembled hollow sphere shaped Bi_2WO_6/RGO composites for efficient sunlight-driven photocatalytic degradation of organic pollutants. Chem Eng J 316:778–789

[27] Schneider J, Matsuoka M, Takeuchi M, Zhang J, Horiuchi Y, Anpo M, Bahnemann DW (2014) Understanding TiO_2 photocatalysis: mechanisms and materials. Chem Rev 114:9919–9986

[28] Tan Y, Shu Z, Zhou J, Li T, Wang W, Zhao Z (2018) One-step synthesis of nanostructured g-C_3N_4/TiO_2 composite for highly enhanced visible-light photocatalytic H_2 evolution. Appl Catal B 230:260–268

[29] Zuo F, Wang L, Wu T, Zhang Z, Borchardt D, Feng P (2010) Self-doped Ti^{3+} enhanced photocatalyst for hydrogen production under visible light. J Am Chem Soc 132:11856–11857

[30] Cheng Y, Zhang M, Yao G, Yang L, Tao J, Gong Z, He G, Sun Z (2016) Band gap manipulation of cerium doping TiO_2 nanopowders by hydrothermal method. J Alloys Compd 662:179–184

[31] Hwang YJ, Yang S, Lee H (2017) Surface analysis of N-doped TiO_2 nanorods and their enhanced photocatalytic oxidation activity. Appl Catal B 204:209–215

[32] Yan X, Xing Z, Cao Y, Hu M, Li Z, Wu X, Zhu Q, Yang S, Zhou W (2017) In-situ C-N-S-tridoped single crystal black $TiO2$ nanosheets with exposed 001 facets as efficient visible-light-driven photocatalysts. Appl Catal B 219:572–579

[33] Zhang X, Wang Y, Liu B, Sang Y, Liu H (2017) Heterostructures construction on TiO_2 nanobelts: a powerful tool for building high-performance photocatalysts. Appl Catal B 202:620–641

[34] Kwon Kaang B, Han N, Jang W, Young Koo H, Boo Lee Y, San Choi W (2018) Crossover magnetic amphiprotic catalysts for oil/water separation, the purification of aqueous and non-aqueous pollutants, and organic synthesis. Chem Eng J 331:290–299

[35] Kumar A, Kumar A, Sharma G, AaH Al-Muhtaseb, Naushad M, Ghfar AA, Stadler FJ (2018) Quaternary magnetic BiOCl/g-C_3N_4/Cu_2O/Fe_3O_4 nano-junction for visible light and solar powered degradation of sulfamethoxazole from aqueous environment. Chem Eng J 334:462–478

[36] Kumar A, Kumar A, Sharma G, Naushad M, Stadler FJ, Ghfar AA, Dhiman P, Saini RV (2017) Sustainable nano-hybrids of magnetic biochar supported g-C_3N_4/$FeVO_4$ for solar powered degradation of noxious pollutants- Synergism

[37] Liu G, Wang L, Yang HG, Cheng HM, Lu GQ (2010) Titania-based photocatalysts—crystal growth, doping and heterostructuring. J Mater Chem 20:831–843

[38] Giannakas AE, Antonopoulou M, Daikopoulos C, Deligiannakis Y, Konstantinou I (2016) Characterization and catalytic performance of B-doped, B-N co-doped and B–N–F tri-doped $TiO2$ towards simultaneous Cr(VI) reduction and benzoic acid oxidation. Appl Catal B 184:44–54

[39] Teh CY, Wu TY, Juan JC (2015) Facile sonochemical synthesis of N, Cl-codoped TiO_2: synthesis effects, mechanism and photocatalytic performance. Catal Today 256:365–374

[40] Kuvarega AT, Krause RWM, Mamba BB (2015) Evaluation of the simulated solar light photocatalytic activity of N, Ir co-doped TiO_2 for organic dye removal from water. Appl Surf Sci 329:127–136

[41] Wu Y, Dong Y, Xia X, Liu X, Li H (2016) Facile synthesis of N-F codoped and molecularly imprinted TiO_2 for enhancing photocatalytic degradation of target contaminants. Appl Surf Sci 364:829–836

[42] Zhang J, Xiao G, Xiao FX, Liu B (2017) Revisiting one-dimensional TiO_2 based hybrid heterostructures for heterogeneous photocatalysis: a critical review. Mater Chem Front 1:231–250

[43] Quarto FD, Sunseri C, Piazza S, Romano MC (1997) Semiempirical correlation between optical band gap values of oxides and the difference of electronegativity of the elements. Its importance for a quantitative use of photocurrent spectroscopy in corrosion studies. J Phys Chem B 101:333–340

[44] Lv J, Kako T, Li Z, Zou Z, Ye J (2010) Synthesis and photocatalytic activities of $NaNbO_3$ rods modified by In_2O_3 nanoparticles. J Phys Chem C 114:6157–6162

[45] Wang Z, Huang B, Dai Y, Qin X, Zhang X, Wang P, Liu H, Yu J (2009) Highly photocatalytic ZnO/In_2O_3 heterononstructures synthesized by a coprecipitation method. J Phys Chem C 113:4612–4617

[46] Mu J, Chen B, Zhang M, Guo Z, Zhang P, Zhang Z, Sun Y, Shao C, Liu Y (2012) Enhancement of the visible-light photocatalytic activity of In_2O_3-TiO_2 nanofiber heteroarchitectures. ACS Appl Mater Interfaces 4:424–430

[47] Kadi MW, Ismail AA, Mohamed RM, Bahnemann DW (2018) Photodegradation of the herbicide imazapyr over mesoporous In_2O_3-TiO_2 nanocomposites with enhanced photonic efficiency. Sep Purif Technol 205:66–73

[48] Du Q, Ma J, Shao X, Wang W, Tian G (2019) Core-shell structured TiO_2@In_2O_3 for highly active visible-light photocatalysis. Chem Phys Lett 714:208–212

[49] Singh S, Mahalingam H, Singh PK (2013) Polymer-supported titanium dioxide photocatalysts for environmental remediation: a review. Appl Catal A 462–463:178–195

[50] An GW, Mahadik MA, Piao G, Chae WS, Park H, Cho M, Chung HS, Jang JS (2019) Hierarchical $TiO_2@In_2O_3$ heteroarchitecture photoanodes: mechanistic study on interfacial charge carrier dynamics through water splitting and organic decomposition. Appl Surf Sci 480:1–12

[51] Yu H, Ye L, Zhang T, Zhou H, Zhao T (2017) Synthesis, characterization and immobilization of N-doped TiO_2 catalysts by a reformed polymeric precursor method. RSC Adv 7:15265–15271

[52] Cong Y, Zhang J, Chen F, Anpo M (2007) Synthesis and characterization of nitrogen-doped TiO_2 nanophotocatalyst with high visible light activity. J Phys Chem C 111:6976–6982

[53] Yu S, Wu X, Wang Y, Guo X, Tong L (2017) 2D Materials for optical modulation: challenges and opportunities. Adv Mater 29:1606128

[54] Wang F, Feng Y, Chen P, Wang Y, Su Y, Zhang Q, Zeng Y, Xie Z, Liu H, Liu Y, Lv W, Liu G (2018) Photocatalytic degradation of fluoroquinolone antibiotics using ordered mesoporous $g-C_3N_4$ under simulated sunlight irradiation: kinetics, mechanism, and antibacterial activity elimination. Appl Catal B 227:114–122

[55] Xu M, Wang Y, Geng J, Jing D (2017) Photodecomposition of NO_x on Ag/TiO_2 composite catalysts in a gas phase reactor. Chem Eng J 307:181–188

[56] Li Z, Zhang P, Li J, Shao T, Wang J, Jin L (2014) Synthesis of In_2O_3 porous nanoplates for photocatalytic decomposition of perfluorooctanoic acid (PFOA). Catal Commun 43:42–46

[57] Xing MY, Li WK, Wu YM, Zhang JL, Gong XQ (2011) Formation of new structures and their synergistic effects in boron and nitrogen codoped TiO_2 for enhancement of photocatalytic performance. J Phys Chem C 115:7858–7865

[58] Patel N, Jaiswal R, Warang T, Scarduelli G, Dashora A, Ahuja BL, Kothari DC, Miotello A (2014) Efficient photocatalytic degradation of organic water pollutants using V-N-codoped TiO_2 thin films. Appl Catal B 150–151:74–81

[59] Umare SS, Charanpahari A, Sasikala R (2013) Enhanced visible light photocatalytic activity of Ga, N and S codoped TiO_2 for degradation of azo dye. Mater Chem Phys 140:529–534

[60] Zeng L, Lu Z, Li M, Yang J, Song W, Zeng D, Xie C (2016) A modular calcination method to prepare modified N-doped TiO_2 nanoparticle with high photocatalytic activity. Appl Catal B 183:308–316

[61] Ling Q, Sun J, Zhou Q (2008) Preparation and characterization of visible-light-driven titania photocatalyst co-doped with boron and nitrogen. Appl Surf Sci 254:3236–3241

[62] Feng N, Zheng A, Wang Q, Ren P, Gao X, Liu S-B, Shen Z, Chen T, Deng F (2011) Boron environments in B-doped and (B, N)-codoped TiO_2 photocatalysts: a combined solid-state NMR and theoretical calculation study. J Phys Chem C 115:2709–2719

[63] Li Z, Zhang P, Shao T, Wang J, Jin L, Li X (2013) Different nanostructured In_2O_3 for photocatalytic decomposition of perfluorooctanoic acid (PFOA). J Hazard Mater 260:40–46

[64] Zhou W, Du G, Hu P, Li G, Wang D, Liu H, Wang J, Boughton RI, Liu D, Jiang H (2011) Nanoheterostructures on TiO_2 nanobelts achieved by acid hydrothermal method with enhanced photocatalytic and gas sensitive performance. J Mater Chem 21:7937–7945

[65] Zhang W, Xiao X, Li Y, Zeng X, Zheng L, Wan C (2016) Liquid-exfoliation of layered MoS_2 for enhancing photocatalytic activity of $TiO_2/g-C_3N_4$ photocatalyst and DFT study. Appl Surf Sci 389:496–506

[66] Wei Z, Liang F, Liu Y, Luo W, Wang J, Yao W, Zhu Y (2017) Photoelectrocatalytic degradation of phenol-containing wastewater by $TiO_2/g-C_3N_4$ hybrid heterostructure thin film. Appl Catal B 201:600–606

[67] Wei Z, Liu Y, Wang J, Zong R, Yao W, Wang J, Zhu Y (2015) Controlled synthesis of a highly dispersed $BiPO_4$ photocatalyst with surface oxygen vacancies. Nanoscale 7:13943–13950

[68] Lee H, Choi W (2002) Photocatalytic oxidation of arsenite in TiO_2 suspension: kinetics and mechanisms. Environ Sci Technol 36:3872–3878

[69] Liu W, Wang M, Xu C, Chen S, Fu X (2013) Significantly enhanced visible-light photocatalytic activity of $g-C_3N_4$ via ZnO modification and the mechanism study. J Mol Catal A Chem 368–369:9–15

[70] Scanlon DO, Dunnill CW, Buckeridge J, Shevlin SA, Logsdail AJ, Woodley SM, Catlow CR, Powell MJ, Palgrave RG, Parkin IP, Watson GW, Keal TW, Sherwood P, Walsh A, Sokol AA (2013) Band alignment of rutile and anatase TiO_2. Nat Mater 12:798–801

[71] Xu Y, Schoonen MAA (2000) The absolute energy positions of conduction and valence bands of selected semiconducting minerals. Am Mineral 85:543–556

Publisher's Note Springer Nature remains neutral with regard to jurisdictional claims in published maps and institutional affiliations.